research papers

Optimizing and characterizing grating efficiency for a soft X-ray emission spectrometer

Mark Boots,* David Muir and Alexander Moewes

University of Saskatchewan, 116 Science Place, Saskatoon, Saskatchewan, Canada S7N 5E2.
E-mail: mark.boots@usask.ca

The efficiency of soft X-ray diffraction gratings is studied using measurements and calculations based on the differential method with the S-matrix propagation algorithm. New open-source software is introduced for efficiency modelling that accounts for arbitrary groove profiles, such as those based on atomic force microscopy (AFM) measurements; the software also exploits multi-core processors and high-performance computing resources for faster calculations. Insights from these calculations, including a new principle of optimal incidence angle, are used to design a soft X-ray emission spectrometer with high efficiency and high resolution for the REIXS beamline at the Canadian Light Source: a theoretical grating efficiency above 10% and resolving power $E/\Delta E > 2500$ over the energy range from 100 eV to 1000 eV are achieved. The design also exploits an efficiency peak in the third diffraction order to provide a high-resolution mode offering $E/\Delta E > 14000$ at 280 eV, and $E/\Delta E > 10000$ at 710 eV, with theoretical grating efficiencies from 2% to 5%. The manufactured gratings are characterized using AFM measurements of the grooves and diffractometer measurements of the efficiency as a function of wavelength. The measured and theoretical efficiency spectra are compared, and the discrepancies are explained by accounting for real-world effects: groove geometry errors, oxidation and surface roughness. A curve-fitting process is used to invert the calculations to predict grating parameters that match the calculated and measured efficiency spectra; the predicted blaze angles are found to agree closely with the AFM estimates, and a method of characterizing grating parameters that are difficult or impossible to measure directly is suggested.

Keywords: diffraction grating; grating efficiency; soft X-ray; emission spectrometer.

1. Introduction

On soft X-ray beamlines, the push toward higher-resolution spectroscopy has demanded a new consideration of diffraction grating efficiency. Several recent emission spectrometers (Ghiringhelli *et al.*, 2006; Harada *et al.*, 2012) have been created to offer extremely high resolution resonant inelastic X-ray scattering (RIXS) measurements. However, for these and other photon-hungry techniques, very long count times limit the scientific throughput of their beamlines. The motivation for more efficient monochromators and spectrometers is obvious: to decrease the time required for experiments, or to increase the statistical quality of data gathered in the same time. Higher efficiency also enables previously impossible measurements of weakly emitting and dilute materials, where the detector signals would otherwise fall below the noise floor. Finally, owing to the inevitable trade-off between resolution and efficiency, improvements in efficiency can unlock higher-resolution instrument designs while maintaining adequate signal levels.

Several numerical methods have been developed over the last 30 years to model diffraction grating efficiency: the modal method (Andrewartha *et al.*, 1981; Botten *et al.*, 1981), the differential method (Nevière *et al.*, 1974; Popov & Nevière, 2000, 2001) and the integral method (Maystre, 1972; Pomp, 1991; Goray & Seely, 2002; Goray, 2005). The accuracy and computational performance of each method depend strongly on the application: conducting or non-conducting materials, specific or arbitrary groove shapes, and deep or shallow profiles. Since 1980, the differential method has been applied to the design of soft X-ray monochromators (Nevière *et al.*, 1982; Jark, 1988; Padmore *et al.*, 1994), and comparisons with measured efficiencies show good agreement with real gratings as long as the calculated profiles represent the actual gratings (Jark & Nevière, 1987; Bowler *et al.*, 2001). However, in the design of most beamlines, the grating efficiency is still often an afterthought rather than a core driver of the design process.

At the Canadian Light Source we have developed a high-resolution X-ray emission spectrometer for the XES Endstation on the REIXS beamline, currently in commissioning.

Throughout its design, we combined rigorous electromagnetic calculations of the grating efficiency with standard ray-tracing techniques to consider both efficiency and resolution simultaneously. Several operating modes were envisioned to let users choose from different resolution levels, with corresponding trade-offs in efficiency. To calculate the grating efficiencies, we implemented new open-source software based on the classical differential method. The software was validated for physical consistency, and checked against an existing commercial program (*Gradif*). Efficiency calculations produced several insights that guided the design of the machine, including the discovery of an optimal incidence angle for each grating and an efficiency peak in the third diffraction order.

Before installation, the manufactured gratings were characterized using atomic force microscopy (AFM) and diffractometry measurements on beamline 6.3.2 at the Advanced Light Source. Comparisons of the measured and predicted efficiency curves show significant differences that can be explained by physical differences between the ideal and manufactured gratings. (In several cases, this alerted us to serious ruling errors and allowed us to mitigate their impact.) By using a fitting technique to match the measurements to the calculations, we find that it is possible to predict the groove shape, oxide thickness and roughness of real gratings based on efficiency measurements, and that these predictions agree closely with AFM measurements of the actual groove shape.

2. Theory

To calculate grating efficiencies using a full electromagnetic approach, we need to determine the total electric and magnetic fields in the vicinity of a periodic medium, under a known incident field. The *differential method* applies Maxwell's equations in differential form, using a Fourier expansion over the grating period of the fields and the material permittivity. It has been developed incrementally elsewhere (Nevière *et al.*, 1974; Nevière & Montiel, 1996; Popov & Nevière, 2000); here we review the existing theory in sufficient detail to explain our software algorithm.

2.1. Setting up the grating problem on the Fourier basis

Fig. 1 shows an infinite sinusoidal plane wave, propagating inside a uniform non-magnetic medium (Region 2, typically vacuum), incident on another uniform medium (Region 1) with a periodic boundary described by $y_p = g(x)$. Both media are described by their complex permittivity $\tilde{\varepsilon}$ and corresponding refractive index $\nu = c(\mu\tilde{\varepsilon})^{1/2}$. To simplify to two dimensions, the grating is assumed invariant in the z-direction (out of the page), and the incident plane wave propagates along a wavevector $\mathbf{k}_2$ contained within the xy plane. The incident electric field

$$\begin{aligned}\mathbf{E}_{\text{incident}} &= \mathbf{A}\exp\left[i(\mathbf{k}_2\mathbf{r} - \omega t)\right]\\ &= \mathbf{A}\exp\left[ik_2(x\sin\theta_2 - y\cos\theta_2)\right]\exp(-i\omega t),\end{aligned}$$
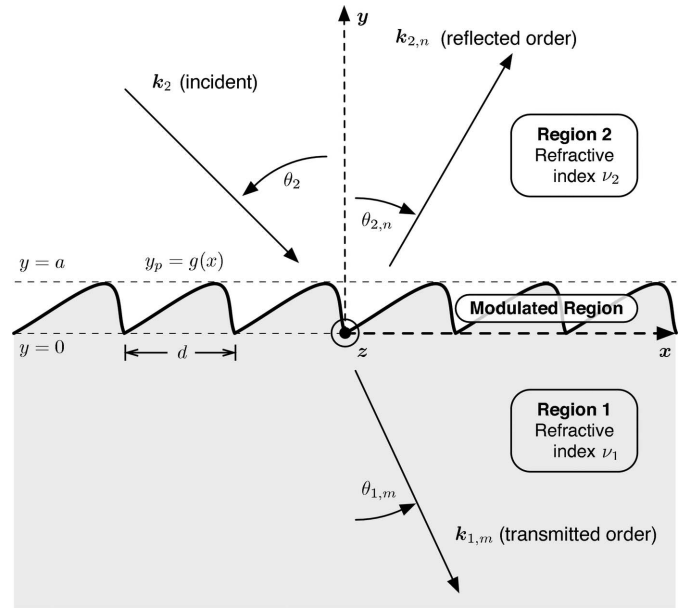

Figure 1
Wavevectors in the in-plane incidence condition for a simple grating. Subscripts 1, 2 or superscripts (1), (2) are used to designate the region. Our sign convention for the incidence angle θ_2 and the reflected and transmitted diffraction angles $\theta_{2,n}$, $\theta_{1,m}$ uses positive angles in the directions shown.

with wavenumber $k_2 = |\mathbf{k}| = \nu_2\omega/c$, has arbitrary polarization described by complex vector $\mathbf{A}$; however, it can always be decomposed into two independent components. The transverse electric (TE) component has an electric field parallel to the z-axis: $\mathbf{E} = E_z\hat{\mathbf{z}}$. The transverse magnetic (TM) component has its magnetic field parallel to the grooves: $\mathbf{H} = H_z\hat{\mathbf{z}}$. This decomposition allows solving the problem separately for each polarization, and then superposing the outgoing fields based on the components of the incident wave. Because all fields have the same harmonic dependence on $\exp(-i\omega t)$, this factor is omitted but implied in subsequent equations.

The source-free Maxwell equations in differential form ($\nabla \times \mathbf{E} = -\partial\mathbf{B}/\partial t$, $\nabla \times \mathbf{B} = \mu\varepsilon\partial\mathbf{E}/\partial t$) can be solved simultaneously for each polarization (Nevière & Popov, 2003), giving the wave equations

$$\nabla^2 E_z + k^2 E_z = 0 \qquad \text{(TE)}, \tag{1}$$

$$\nabla\left[\frac{1}{k^2}\nabla H_z\right] + H_z = 0 \qquad \text{(TM)}, \tag{2}$$

where $k^2 = k^2(x, y)$ is the squared impedance of the material as a function of position: $k = k_2 = \nu_2\omega/c$ above the grating, and $k = k_1 = \nu_1\omega/c$ inside the grating material.

Within the modulated region, $k = k(x, y)$ varies whether inside or outside of a groove. Above and below the modulated region ($y > a$ and $y < 0$), k^2 is constant and both equations reduce to the Helmholtz equation

$$\nabla^2 u_z + k^2 u_z = 0, \tag{3}$$

with $u_z = E_z$ for TE and $u_z = H_z$ for TM.

For an infinite incident wave, the periodicity of the boundary conditions over the grating period d introduces a pseudo-periodic relationship for the field (Nevière *et al.*, 1974),

$$u_z(x + d, y) = \exp(ik_2 d \sin \theta_2) u_z(x, y)$$
$$= \exp(i\alpha_0 d) u_z(x, y),$$

where $\alpha_0 \equiv k_2 \sin \theta_2$. Then, defining $\alpha_n \equiv \alpha_0 + 2\pi n/d$, the total field can be represented by the pseudo-Fourier expansion,

$$u_z(x, y) = \sum_{n=-\infty}^{\infty} u_n(y) \exp(i\alpha_n x), \tag{4}$$

which must ultimately be truncated to $n = \pm N$ for numerical calculations.

In the homogeneous regions, inserting this expansion into the Helmholtz equation (3) allows an analytic solution. For each n, the Fourier coefficients have the solution

$$u_n(y) = A_n \exp(-i\beta_n y) + B_n \exp(i\beta_n y),$$

where

$$\beta_n = \left(k^2 - \alpha_n^2\right)^{1/2},$$

and A_n and B_n are unknown constants to be determined by additional boundary conditions.

The nature of the total field depends on the region. In Region 2 above the grooves, there is only a single downgoing (incident) plane wave A_0. The upgoing field (B_n terms) consists of a finite sum of propagating plane waves for all n where $\beta_n^{(2)}$ is real, and an infinite sum of decaying plane waves [when $\beta_n^{(2)}$ is complex],

$$u_z(x, y) = A_0^{(2)} \exp\left[i\alpha_0 x - i\beta_0^{(2)} y\right]^{1/2}$$
$$+ \sum_{n=-\infty}^{\infty} B_n^{(2)} \exp\left[i\alpha_n x + i\beta_n^{(2)} y\right]^{1/2}. \tag{5}$$

The diffraction grating's *reflected orders* appear in this expansion as the finite set of n values and $B_n^{(2)}$ terms that create propagating plane waves travelling away from the grating. Now n can be identified with the *diffraction order*, and this expression is known as the *Rayleigh expansion* for the diffracted field (Nevière & Popov, 2003).

In Region 1 below the grooves, the grating material is absorbing, so the refractive index and $k = k_1$ are complex. Eliminating upgoing waves incident from below the grating provides the Rayleigh expansion for the transmitted field ($y \leq 0$), corresponding to the *transmitted orders*,

$$u_z(x, y) = \sum_{n=-\infty}^{\infty} A_n^{(1)} \exp\left[i\alpha_n x - i\beta_n^{(1)} y\right]. \tag{6}$$

2.2. The grating equation and efficiencies

Each propagating term in the Rayleigh expansions is an outgoing plane wave. Equating the x-component of the reflected wavevector $\mathbf{k}_{2,n}$ with the x-component of the

expansion gives the well known *grating equation* for the *diffraction angle* $\theta_{2,n}$ of the reflected order n,

$$n\lambda/d = \sin \theta_{2,n} - \sin \theta_2.$$

However, the relative intensity of each order is given by the still-unknown expansion coefficients: $B_n^{(2)}$ for the reflected orders, and $A_n^{(1)}$ for the transmitted orders. The *grating efficiency* of each order, defined as the ratio of the power of the outgoing wave through a constant area above the grating relative to the incident wave, is related through the time-averaged Poynting vector. The result (Nevière *et al.*, 1974) shows that the efficiency of the reflected orders $e_n^{(r)}$ is directly related to the $B_n^{(2)}$ coefficients,

$$e_n^{(r)} = B_n^{(2)} B_n^{(2)*} \beta_n^{(2)} / \beta_0^{(2)}. \tag{7}$$

2.3. Solving the field within the grooves

Finding these coefficients requires numerical techniques to solve the field within the modulated region between $y = 0$ and $y = a$. Equation (4) still applies, but unlike the Rayleigh expansions the expansion is now a function of y. At a fixed y, the impedance $k^2(x, y)$ is a step function that depends on the shape of the profile, going from k_2^2 outside the groove to k_1^2 inside the groove. This function is also periodic on $(x \rightarrow x + d)$, so it can be expressed by another Fourier expansion,

$$k^2(x, y) = \sum_{n=-\infty}^{\infty} k_n^2(x, y) \exp(2\pi i n x/d), \tag{8}$$

which can be computed based on the groove geometry, either analytically (Nevière *et al.*, 1974) or using the fast Fourier transform algorithm.

The goal is to find a numerical solution for the general wave equation (1) in the Fourier basis that satisfies the boundary condition of matching the Rayleigh expansions at $y = 0$ and $y = a$. Because the boundary conditions are different for TE and TM polarization, we show only the TE case here; the more complicated TM solution is described by Popov & Nevière (2000).

Putting the expansions for the field [equation (4)] and the impedance [equation (8)] into equation (1) gives a set of second-order differential equations, one for each n, captured in the matrix notation,

$$\frac{d^2[u(y)]}{dy^2} = M(y)[u(y)], \tag{9}$$

where we define the column vector $[u(y)]$ with the $2N + 1$ components $u_n(y)$. The $(2N + 1) \times (2N + 1)$ square matrix $M(y)$ must be calculated at each y value,

$$M_{nm}(y) = -k_{(n-m)}^2(y) + \alpha_n^2 \delta_{nm};$$

$$\tag{10}$$

$$\delta_{nm} = \begin{cases} 1 & \text{if } n = m, \\ 0 & \text{if } n \neq m. \end{cases}$$

This represents a set of $(2N + 1)$ boundary value problems (BVPs). In TE polarization, the boundary conditions are derived from the continuity of the tangential component of the electric field and the normal component of the magnetic field at $y = 0$ and $y = a$; they provide a relationship to the Rayleigh coefficients,

$$u_n(a) = A_0^{(2)} \exp\left[-i\beta_0^{(2)}a\right]\delta_{n,0} + B_n^{(2)} \exp\left[i\beta_n^{(2)}a\right], \quad (11)$$

$$u'_n(a) = -i\beta_0^{(2)}A_0^{(2)} \exp\left[-i\beta_0^{(2)}a\right]\delta_{n,0} + i\beta_n^{(2)}B_n^{(2)} \exp\left[i\beta_n^{(2)}a\right], \quad (12)$$

$$u_n(0) = A_n^{(1)}, \quad (13)$$

$$u'_n(0) = -i\beta_n^{(1)}A_n^{(1)}. \quad (14)$$

However, because the Rayleigh coefficients are still unknown, these do not provide direct boundary values for the $u_n(y)$ function, only a link between the function and its derivative. In this situation an algorithm related to the *shooting method* is used to solve the BVP.

2.3.1. The simple shooting method. Because the differential equation is a linear system, we can construct a general solution that matches the boundary conditions out of a linear combination of trial solutions. The Fourier expansion for the field represents a complete basis, so we can use it to generate a complete set of $2N + 1$ trial solutions $[\tilde{u}(y)]_p$ for the vector $[u(y)]$, where $p = [-N, N]$. Any orthogonal set of particular solutions that satisfies the boundary conditions at $y = 0$ [equation (14)] is acceptable, so we choose the following values for the pth trial solution at $y = 0$ (Nevière *et al.*, 1974),

$$\tilde{u}_n(0)_p = \delta_{p,n}, \quad (15)$$

$$\tilde{u}'_n(0)_p = -i\beta_n^{(1)}\delta_{p,n}. \quad (16)$$

This transforms the $2N + 1$ boundary value problems into $(2N + 1) \times (2N + 1)$ initial value problems. All of the trial solutions can now be individually integrated from $y = 0$ to $y = a$, using equation (9),

$$[\tilde{u}''(y)]_p = M(y)[\tilde{u}(y)]_p,$$

by a reliable numerical integration algorithm.

With the integration complete, we seek a linear superposition of trial solutions that satisfies the boundary conditions at $y = a$ [equations (11) and (12)],

$$\sum_{p=-N}^{+N} c_p\tilde{u}_{np}(a) = A_0^{(2)} \exp\left[-i\beta_0^{(2)}a\right]\delta_{n,0}$$
$$+ B_n^{(2)} \exp\left[i\beta_n^{(2)}a\right], \quad (17)$$

$$\sum_{p=-N}^{+N} c_p\tilde{u}'_{np}(a) = -i\beta_0^{(2)}A_0^{(2)} \exp\left[-i\beta_0^{(2)}a\right]\delta_{n,0}$$
$$+ i\beta_n^{(2)}B_n^{(2)} \exp\left[i\beta_n^{(2)}a\right]. \quad (18)$$

Because of the boundary condition at $y = 0$ [equation (13)] and our choice of starting values [equation (15)], the superposition

constants c_p can be identified with the coefficients $A_n^{(1)}$, as $c_p = A_n^{(1)}$ for $n = p$. Therefore, these represent $2(2N + 1)$ linear equations for the $2(2N + 1)$ unknowns $A_n^{(1)}$, $B_n^{(2)}$, which can be solved using standard techniques of linear algebra. Finally, with the outgoing field fully determined, we compute the efficiency for each order using equation (7).

2.4. Numerical challenges

The differential method presented so far is rigorous in that no approximations, other than the assumption of periodicity, have been made. However, there are two challenges associated with its implementation.

2.4.1. Truncation and convergence. Practical computations must obviously truncate the Fourier sums to finite values of $\pm N$; for functions with step discontinuities, this can be problematic. Generally, the minimum acceptable truncation index would be identified through convergence testing, where repeated calculations with larger values of N are found to produce identical results. However, equations (9) and (10) are based on the convolution theorem: where $h(x) = f(x)g(x)$, the Fourier coefficients of $h(x)$ are

$$h_n = \sum_{m=-\infty}^{+\infty} f_{(n-m)}g_m. \quad (19)$$

This is valid when the sums are carried to infinity, but it is not clear that it applies to truncated sums. The theoretical work of Li (1996*b*) examined the convergence of products of truncated Fourier series when the individual functions (for example, the field coefficients u_n and the impedance k^2) had coincident or non-coincident discontinuities. For TE polarization, the tangential electric field E_z and its first derivative are continuous at the boundary of the grating. In this situation the product is also continuous and convergence is achieved with low values of N; usually 15 to 45 for typical soft X-ray gratings. In the case of TM polarization (not shown), the electric field is normal to, and therefore discontinuous at, the boundary of the grating. This resulted in convergence problems for many years, until a reformulation of equation (19) appropriate for functions with coincident discontinuities was suggested (Li, 1996*b*). The result, applied to the differential method, has been referred to as the fast Fourier factorization method and is described by Popov & Nevière (2000) and Nevière & Popov (2003).

2.4.2. Growing exponentials and the S-matrix algorithm. The numerical solution of the differential equations described in §2.3.1 must integrate growing exponential functions over the distance from $y = 0$ to $y = a$. For deep gratings, the numerical values become very large; however, the final values of B_n, which must be below unity for physically realistic efficiencies, are computed as differences of products of these large exponential functions. For computer arithmetic using standard double-precision floating-point variables, the loss of significance leads to meaningless results.

To mitigate this problem, extended precision variables can be used, but this is computationally slow and only extends the maximum depth of gratings that can be calculated. Instead, a

deep grating can be divided into slices of horizontal layers, such that each layer is thin enough to avoid loss of significance. Within each layer, $2(2N + 1)$ orthogonal trial solutions for upgoing and downgoing waves are integrated from the bottom to the top of the layer. (This constitues a *multiple shooting* method.) The values for all trial solutions at the top of the layer give the *T-matrix* describing the effect of that layer on the Rayleigh coefficients above and below it. It would be possible to calculate the *T-matrix* for the entire grating as the matrix product of all the layers; however, this produces the same large numerical values we need to avoid. Instead, the *S-matrix* algorithm (Li, 1996a) uses algebraic manipulation to re-arrange the matrix multiplications so that the products of the growing exponentials never appear in the result; a stable recursive algorithm is used to compute the cumulative effect of each layer on the entire stack below it. Once the *S*-matrix for the entire stack is computed, the B_n coefficients are extracted from it. Detailed application of the *S*-matrix to the differential method can be found by Nevière & Montiel (1996) and Nevière & Popov (2003).

With this modification in place, we find that efficiencies calculated using the differential method are in excellent agreement with measurements of the soft X-ray gratings shown in §6.

2.5. Refractive indexes for grating materials and soft X-rays

The differential method assumes that the grating material is not perfectly conducting, so that it can be described by a complex refractive index $\nu(\lambda) = n + i\kappa$. (The real part n describes the dielectric strength and related phase velocity within the material; the extinction coefficient κ describes the attenuation.) For soft X-rays, the light frequency is higher than the plasma frequency in metals, so both metals and conventional dielectrics behave as absorbing weak dielectrics; the assumption is therefore acceptable. For many materials at soft X-ray wavelengths, n is smaller than but approximately unity, so the refractive index is listed as

$$\nu = 1 - \delta + i\kappa.$$

To determine refractive indexes for materials as a function of wavelength, we use the semi-empirical database of atomic scattering factors gathered by Henke *et al.* (1993). The complex refractive index for a compound material can be determined from the scattering factors of the constituent atoms as

$$\tilde{n} = 1 - \delta - i\beta = 1 - \frac{r_e}{2\pi}\lambda^2 \sum_{q=1}^{Q} n_q f_q(0),$$

where there are Q different types of atoms in the material, n_q is the number density of atoms of type q, $f_q(0)$ is the tabulated complex forward scattering factor $f(0)$ for atom q, and r_e is the classical electron radius (Henke *et al.*, 1993). (Note that the refractive index $\tilde{n}$ here uses the opposite sign convention to ν defined above; $\nu = \tilde{n}^*$.)

Using this method to calculate the refractive index assumes that the photoabsorption cross section does not depend on the bonding environment of atoms in the material; *i.e.* it assumes that the individual atoms scatter independently as dipoles. In the vicinity of absorption edges, two processes invalidate this assumption: transitions to weakly bound excited states produce fine structure near the absorption edge (NEXAFS), and backscattering of outgoing photoelectrons from the atoms in a crystal causes oscillations above the edge (EXAFS) (Henke *et al.*, 1993). Therefore, the refractive indexes and corresponding efficiencies we calculate are not expected to be accurate in the vicinity of absorption edges.

3. Computer implementation

In the initial design of the XES endstation, we used a commercial implementation of the differential method called *Gradif*, sold by M. Nevière (2003). Recently, the need for higher performance during optimization and fitting inspired us to write our own implementation, designed specifically to exploit multi-core processors and high-performance computing (HPC) resources. Unlike previous implementations of the differential method, it can handle arbitrary groove profiles, including those generated from AFM measurements of the actual groove shape, in addition to standard profiles (rectangular, blazed, trapezoidal and sinusoidal). The *S*-matrix propagation algorithm is used to allow deep gratings, with automatic determination of the number of layers required. The ODE integration is performed using an Adams–Bashforth multi-step method (Byrne & Hindmarsh, 1975) with adaptive step sizes, which provides high performance and stability. Gratings can consist of a bare modulated substrate like the one in Fig. 1, or they can have a thick or thin (inter-penetrating) coating of a different material. A database of common materials is included for automatic look-up of the refractive index as a function of wavelength, based on the Henke scattering factors. To generate efficiency spectra, the program provides three scanning modes: (i) scans over a range of wavelengths at constant incidence, (ii) scans over a range of incident angles at a constant wavelength, or (iii) scans over a range of wavelengths while maintaining a constant included angle from the incident to the diffracted beam ('monochromator mode').

The solver supports fine parallelization of a single efficiency calculation over multiple processor cores, and the command-line program also features coarse parallelization of calculations over nodes in a HPC cluster.

Currently, the new software only calculates the TE efficiency; work is ongoing to implement TM calculations. For most soft X-ray applications, this is not a major limitation because the TE and TM efficiencies converge at grazing incidence, and, despite small differences in absolute values, the shapes of the efficiency spectra are similar. Therefore, designers will not be misled when using TE calculations to optimize grazing-incidence optics for TM or mixed polarization light.

The new software was validated for consistency with physical principles. For non-absorbing gratings (*i.e.* materials with real refractive indexes), the sum of all the transmitted

and reflected efficiencies must be unity. For absorbing gratings, this sum is always less than unity. The Helmholtz reciprocity principle provides another test: applied to optics, it requires that the quantity of light transmitted be unaffected under interchange of the source and detector (Jark, 1988). For general gratings, an analytic proof shows the efficiency of a diffracting order n under incidence angle θ_1 and outgoing angle θ_2 must be the same as the efficiency under incidence $-\theta_2$ and outgoing angle $-\theta_1$ (Maystre & McPhedran, 1974). All of these requirements were confirmed in testing. Additional self-consistency checks were performed: results for thin gratings using single and multiple layers in the S-matrix method were identical, and the arbitrary groove profile mode produced identical results when used to define standard profiles. Finally, the new software was tested for consistency with the commercial *Gradif* program. Depending on the numerical accuracy requested from each program, the agreement is typically better than three significant figures.

The new implementation has been released under an open-source license for others to use and extend as required; the code and documentation can be found at http://github.com/markboots/peg. Beamline designers can either download the code or they can access it through our online calculator at http://www.dgembe.com/ for simple calculations of grating efficiency over a range of wavelengths or incidence angles. Work is ongoing to add more advanced optimization features to the online application.

4. Application to instrument design

4.1. Factors affecting the grating efficiency

We used the software to survey trends in the factors that affect grating efficiency: substrate and coating material, coating thickness, groove density, groove shape and geometry, incidence angle, and wavelength. Several of our conclusions from these surveys are well known, such as the fact that:

(i) Blazed gratings with facets that 'reflect' light in the direction of the desired order significantly outperform rectangular and sinusoidal gratings, as long as the incidence angle and wavelength remain close to the on-blaze condition (Johnson, 1978; Palmer & Loewen, 2005).

(ii) Increasing the groove density always reduces the maximum efficiency.

(iii) Coating materials of light elements like carbon and nickel offer high peak reflectivity but also have strong absorption edges in the soft X-ray range, whereas heavy elements like gold, platinum and iridium offer lower but near-constant reflectivity.

(iv) Owing to short penetration depths, coating thicknesses of ∼50 nm or more are indistinguishable from infinitely thick gratings of the same material.

Other results provided surprising insights for instrument design, as follows.

4.1.1. Optimal incidence angles. The reflectivity of plain mirrors increases monotonically as a function of incidence angle when approaching grazing incidence; we might expect
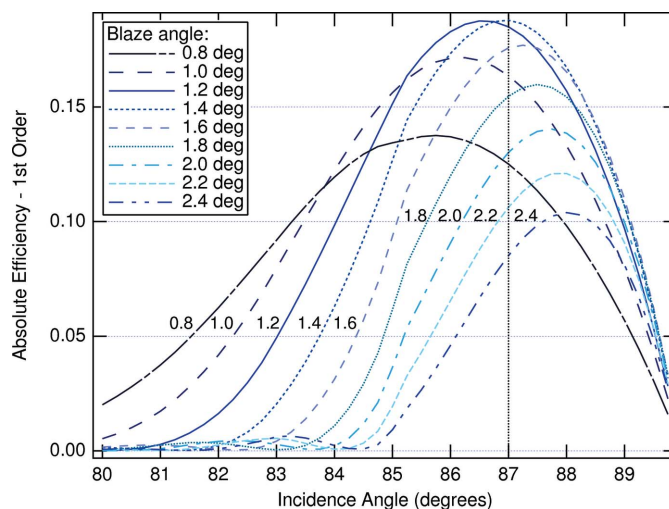

Figure 2
First-order efficiency as a function of blaze angle and incidence angle. The blaze angle can always be adjusted to optimize the efficiency for a given incidence angle. However, there exists an optimal incidence angle (and corresponding blaze angle) where the highest possible efficiency is achieved. Grating: 1200 lines mm^{-1}, blazed profile, platinum coating; photon energy: 400 eV.

the same to apply for diffraction gratings. While this is true in the $n = 0$ diffraction order, we find that for all useful orders there is an optimal incidence angle below 90° that maximizes efficiency. This is important in instrument design, since using higher (more grazing) incidence reduces the amount of light captured by the grating and hence the *geometric* efficiency.

If a certain arbitrary incidence angle is required for other reasons, the groove geometry, *i.e.* the blaze angle for blazed gratings and the groove depth for rectangular and sinusoidal gratings, can always be adjusted to maximize efficiency at that incidence. However, Fig. 2 shows that when the geometry parameters are optimized simultaneously for each incidence the absolute maximum efficiency occurs at a specific optimal angle. [This approach differs from the efficiency maps of Jark (1988), where the blaze angle was kept constant as the wavelength and incidence were varied. Here we seek to optimize the incidence and blaze angle for every wavelength.]

We conducted more calculations to determine that this optimal incidence depends only on the groove density and wavelength. For rectangular gratings, the optimal incidence angle for the first inside order ($n = -1$) occurs at the $n = +1$ *Wood anomaly*. (This happens when the first outside order goes from propagating to evanescent; intuitively, it makes sense that its energy must be re-distributed, increasing the efficiency of the remaining propagating orders.) Therefore, the optimal incidence $\theta_{i,max}$ can be computed from the grating equation by setting the diffraction angle for the +1 order to 90°,

$$\sin \theta_{i,max} = 1 - \lambda/d.$$

Fig. 3 plots the optimal incidence angle for rectangular gratings as a function of groove density and wavelength, determined through global optimization of the incidence and groove geometry. It shows that the optimal angle tracks the
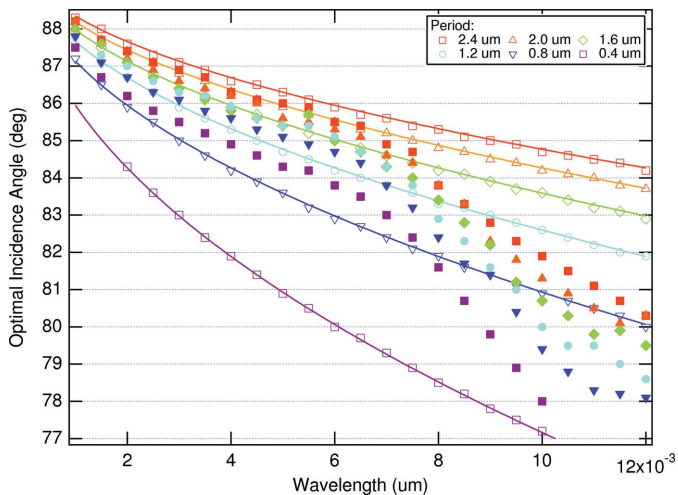
Figure 3

The optimal incidence angle depends on the groove period and the wavelength. Solid lines are the calculated angles for the $n = +1$ Wood anomaly where the first outside order becomes evanescent. Markers represent optimal incidence angles for first inside order efficiency found using global optimization of the groove geometry and incidence to $\pm 0.1°$. Open markers: rectangular profile. Filled markers: blazed profile.

analytic formula within the accuracy of the global optimization ($\pm 0.1°$).

The situation for blazed gratings is different. Here, the optimal incidence angle cannot be predicted analytically by the Wood anomaly. We currently cannot offer a simple formula for the optimal incidence of blazed gratings; a full numerical optimization is required to find it.

Using the Wood anomaly explanation might suggest that the efficiency advantage gained through this technique would be lost as soon as the incidence angle or wavelength changes enough for the first outside order to begin propagating. Instead, we find that this does not happen; the peak width of the optimization is wide enough to use in practical designs over a range of wavelengths or incidence angles.

The optimal incidence angle provides a useful starting point when designing fixed-incidence instruments, such as the emission spectrometer on the REIXS XES endstation. Depending on the wavelength range and other constraints, it might also be useful for variable-incidence instruments (constant-deviation monochromators, *etc.*).

4.1.2. Third-order operation. Typically, the grating efficiency decreases significantly for higher orders, so most instruments operate in the $n = -1$ order. Previous soft X-ray research has calculated low efficiencies in the third order, and measured efficiencies that were even lower (Jark & Nevière, 1987), which were attributed to profile irregularities. However, while attempting to maximize the resolution of the REIXS XES spectrometer, we discovered a useful efficiency peak in the third diffraction order. We therefore added two additional gratings, optimized intentionally for operation in the third order, to provide a special high-resolution mode.

The justification for this decision is shown in Fig. 4. To increase the resolution of the machine without exceeding the space constraints of the beamline, two hypothetical alternatives could provide equivalent resolution: one could (i)
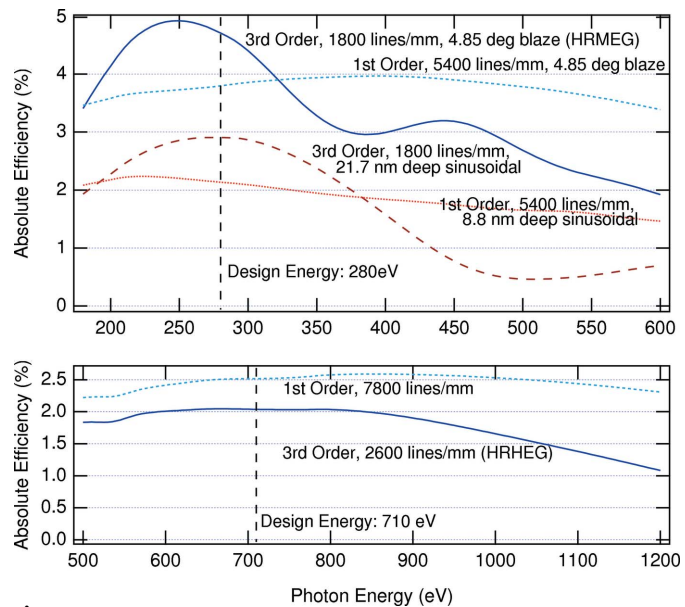

Figure 4

The justification for our third-order instrument design: the same resolution can be achieved using the third order, or using another grating with three times the groove density in the first order. When optimizing for 280 eV (top) we find that a properly optimized 1800 lines mm^{-1} grating in the third order has higher efficiency than the optimized 5400 lines mm^{-1} grating in the first order. This is true for sinusoidal (red) as well as blazed profiles (blue). When optimizing for 710 eV (bottom), the third-order grating has comparable but slightly lower efficiency than the first-order alternative. However, it would be impossible to rule a 7800 lines mm^{-1} grating with acceptable quality, so the third-order grating is the only practical choice.

triple the groove density of the grating, or (ii) use the third diffraction order at the original groove density.

Fig. 4 includes an example optimized for 280 eV. When all grating parameters are optimized for operation in the intended order, the third-order grating with 1800 lines mm^{-1} actually has higher efficiency than its triple-density equivalent (5400 lines mm^{-1}) in the first order. This applies even for sinusoidal as well as blazed profiles. In another example optimized at 710 eV, the third-order grating (2600 lines mm^{-1}) has slightly lower but comparable efficiency with the first-order version (7800 lines mm^{-1}).

In practice, the third-order alternative is actually the only option: it would be almost impossible to manufacture gratings for the first-order designs with such high groove densities. (Even if the grating could be ruled, the expected low quality would reduce its real-world efficiency.) For the REIXS instrument, the third-order design is the only option to achieve such high resolution without extending the physical size of the machine. With proper blazing, the predicted efficiencies are low but usable ($\sim 2\%$).

4.2. Design process for the REIXS XES endstation

The design process for the new spectrometer considered the interplay between factors affecting resolution and efficiency; it will be described alongside initial experimental results in a forthcoming paper. Here we summarize some of the principles determined from efficiency studies.

Table 1
Gratings chosen for the REIXS spectrometer, with target energies used for optimization, accessible energy ranges, and optimized nominal grating parameters.

Grating	Optimization energy (eV)	Energy range (eV)	Groove density (lines mm^{-1})	Incidence angle (°)	Coating	Blaze angle (°)
First order						
Low energy (LEG)	92 eV (Si)	30–300	600	86	Au	1.85
Impurity (IMP)	400 eV (N)	75–750	900	87	Ni	1.11
Medium energy (MEG)	400 eV (N)	250+	1200	88	Ni	1.48
High energy (HEG)	719 eV (Fe)	400+	2000	88	Pt	1.52
Third order						
High-resolution medium energy (HRMEG)	280 eV (C)	280+	1800	88	Ni	4.85
High-resolution high energy (HRHEG)	719 eV (Fe)	525+	2600	88.25	Pt	4.05

The design goals for the spectrometer were to provide a 'workhorse' instrument with excellent performance at specific emission lines of interest to many research groups: Si $L\beta$ (92 eV), C, N and O $K\alpha$ (277, 392, 525 eV) lines, along with good performance at many transition-metal L and rare-earth M lines (600–1100 eV). Blazed gratings were chosen based on significantly higher ($\times2$) efficiency, but had to be optimized for each wavelength; initially, we proposed using a separate optimized grating for each edge of interest. Many of these were found to be overlapping in performance, so the total number was reduced to include only the LEG, MEG and HEG gratings described in Table 1. A fourth 'impurity' grating (IMP) was added to offer a high-efficiency low-resolution mode over a wide wavelength range for studying dilute samples. The incidence angles for each grating were chosen using the optimal incidence principle (above) as a starting point, and refined based on focusing constraints and ray-tracing results. Finally, we added two gratings (HRMEG, HRHEG) optimized for third-order operation to enable very high resolution RIXS studies.
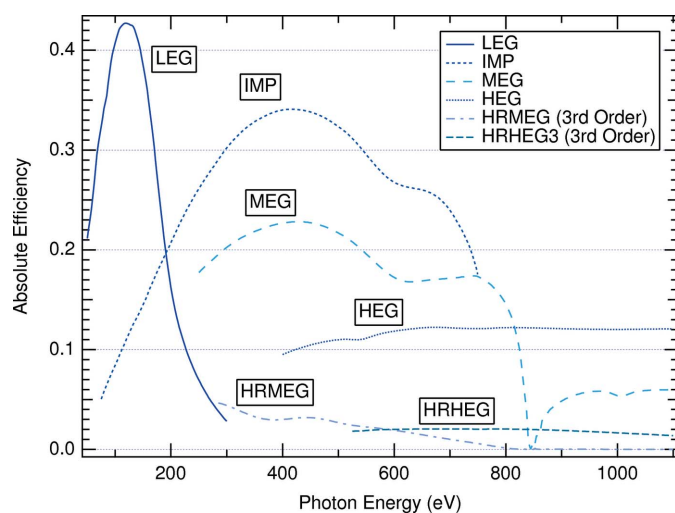

Figure 5
Theoretical (calculated) efficiency spectra for the gratings in the REIXS XES spectrometer, over their intended ranges of operation. Using the LEG, MEG and HEG, we achieved our goal of >10% efficiency from 100 to 1000 eV. The IMP grating provides high efficiency at low resolution over a wide wavelength range, and the two third-order gratings provide a very high resolution mode.

The groove geometries and coatings were all optimized using efficiency calculations; Table 1 lists the relevant parameters for each grating. Fig. 5 plots the predicted nominal efficiencies over each grating's usable energy range.

5. Characterization of grating parameters and efficiency

The spectrometer gratings were fabricated by Bach Research Corporation using mechanical ruling. All the gratings were ruled in a gold layer on a fused silica substrate; nickel or platinum coatings were subsequently evaporated for all except the LEG. Before installing the gratings in the spectrometer, we characterized their actual groove profile and efficiency.

5.1. Profile measurements using AFM

The surfaces of the gratings were characterized using AFM. Measurements were taken in non-contact (tapping) mode at two locations (centre and edge) on each grating, with each image covering between five and ten groove periods (Fig. 6). The measurements were conducted at the Center for X-ray Optics at the Lawrence Berkeley National Laboratory (LBNL), using a reference sample to calibrate the scaling of the z-axis for realistic estimates of the blaze angles. The grating cross sections were integrated over the width of the image to produce an average groove profile, shown in Fig. 6. From the averaged profiles, we fitted the slopes of each groove to provide an estimate of the blaze angles (Table 2).

5.2. Efficiency measurements using the beamline 6.3.2 diffractometer

The efficiencies of the gratings as a function of wavelength ('efficiency spectra') were measured on the Calibration and Standards Beamline (6.3.2) at the Advanced Light Source, LBNL. This bending-magnet beamline provides synchrotron radiation through a monochromator with a resolving power ($\lambda/\Delta\lambda$) of approximately 7000 (Underwood *et al.*, 1996). Interchangeable filters of different elements are used to suppress higher-order radiation from the monochromator and calibrate the wavelength. On reaching the grating, the light is 90% linearly polarized perpendicular to the plane of incidence, which is ideal for comparison with the TE efficiency calculated by our software.
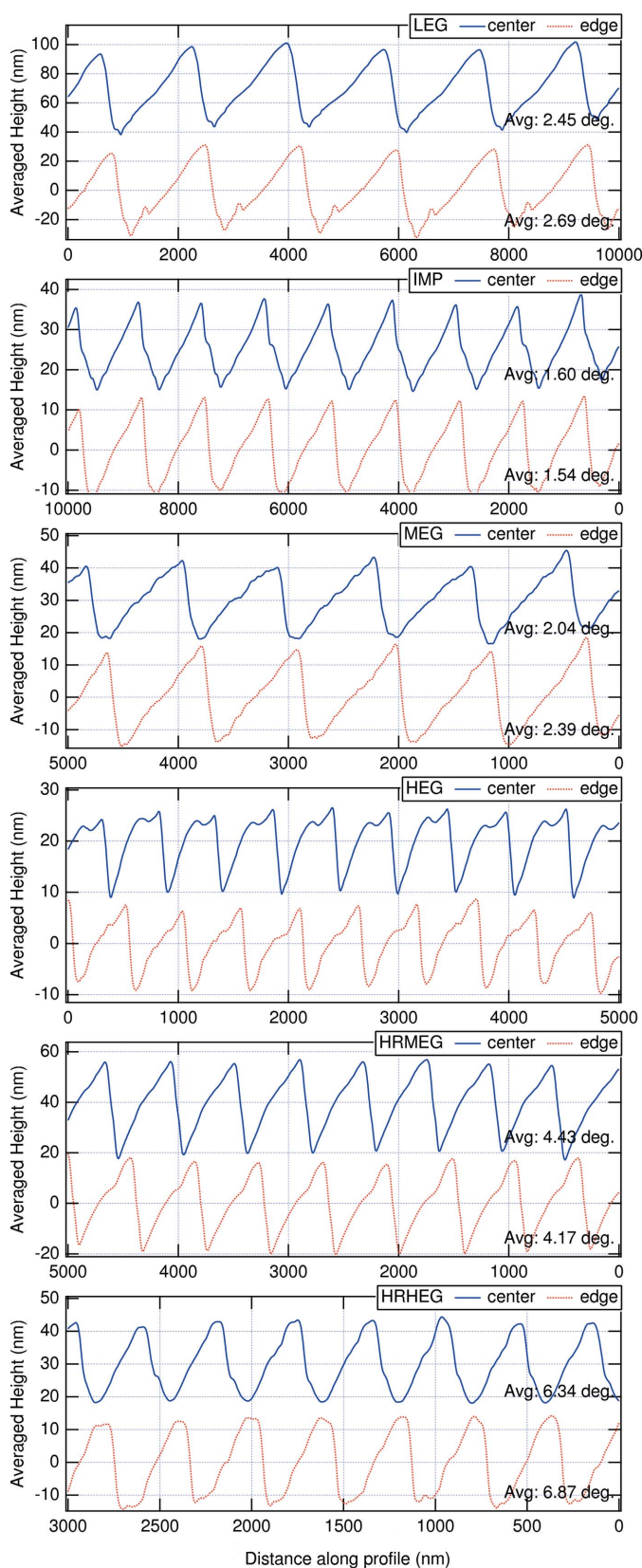
Figure 6
Groove profiles for all of the REIXS XES gratings, generated by integrating calibrated AFM image data along the grooves. A separate AFM image was measured at the centre and edge of each grating.

Table 2
Comparison of nominal and fitted grating parameters, using fitting to match the calculated efficiency spectra to the measured curves. The predicted (Fit) blaze angles agree very closely with estimates from AFM measurements.

	Blaze angle (°)			Roughness	Oxide thickness
	Nominal	Fit	AFM estimate	Fit (nm)	Fit (nm)
LEG	2.26	2.35	2.45 ± 0.20	0.025	N/A
IMP	1.11	1.65	1.60 ± 0.11	0.5	2.0
MEG	1.48	1.95	2.04 ± 0.22	0.1	1.0

The diffractometer endstation on beamline 6.3.2 provides for the mounting, alignment and measurement of the gratings under test. Independent rotary stages with encoders are used to set the incidence angle of the beam on the grating as well as the outgoing angle to the detector. Multiple detectors are available: gallium arsenide and silicon photodiodes, a CCD camera and a channeltron; we used the Hamamatsu GaAs photodiode. A 2 mm pinhole over the photodiode is standard for grating measurements.

From previous long trace profilometer (LTP) measurements, we knew the actual groove density of each grating with high accuracy. This allowed us to scan the incident wavelength of the beamline while moving the detector angle to keep it centred on the diffraction peak in the order of interest. The efficiency at each wavelength was computed by taking the ratio of the diffracted beam intensity to the direct beam intensity, which was measured in a subsequent scan using the same photodiode. (The scans were normalized using the pre-diffractometer beam intensity I_0, and corrected for dark current of the photodiode.)

6. Analysis and results

6.1. Differences between ideal and manufactured gratings

The measured efficiency spectra are substantially different from our theoretical predictions in Fig. 5. This means that either (a) the theory or software implementation is incorrect, or (b) the gratings we received differ from the nominal specifications. Since there is deviation inherent in any grating manufacturing process, we examine the second possibility before rejecting the theory. Some of the manufacturing differences can be accounted for in revised calculations, while others cannot be modelled using the differential theory.

6.1.1. Blaze angle and groove-shape errors. Errors in the manufactured blaze angle shift the efficiency peaks along the energy/wavelength axis, as well as change the ratio between the first- and second-order peak efficiencies. In general, it is also common for manufactured groove shapes to differ from the triangular, rectangular or sinusoidal ideals. Deviations from the nominal groove geometry can be easily incorporated into the efficiency calculations, as long as they are consistent from groove to groove. When the exact profile is known from AFM measurements, the arbitrary groove profile mode implemented in our software can be used to model any real groove shape.

6.1.2. Oxidation of coatings. Nickel coatings offer theoretically high reflectivity up to 850 eV; however, an oxide layer affects the efficiency significantly, particularly above the O $K\alpha$ edge (543 eV). The software now makes it possible to calculate the efficiency of an oxidized grating by using a thin layer (in our case a layer of NiO) on top of a metal substrate. The detrimental effect of the oxide layer is obvious in the results for the IMP and MEG gratings. This problem can be avoided by evaporating a protective layer of MgF_2 over the nickel coating before exposing the gratings to air. In this case the same calculation technique could be used to model the effect of the MgF_2 coating. The effect of a 1 nm coating is compared with the pure and oxidized nickel efficiency curves in Figs. 8 and 9; it actually increases the theoretical efficiency.

6.1.3. Non-uniform variation in groove shape. During mechanical ruling, variation in the hardness of the metal causes the ruling tip to penetrate shallower or deeper. This causes variation in the groove shape, both along a single groove (across the grating) and from groove to groove. This disrupts the perfect periodicity of the grating, and reduces the constructive interference that forms the diffracted plane waves. The result is an increase in scattered light ('stray radiant energy') and a reduction in efficiency (Palmer & Loewen, 2005). Gratings produced using the holographic method also suffer from aperiodicity, owing to variation in the intensity of the interference pattern used to record the grating (Palmer & Loewen, 2005). However, Johnson (1978) reports that holographic ion-etching methods can produce more uniform profiles with lower scattered light than mechanical ruling, even for blazed gratings.

The assumption of periodicity is fundamental to the differential method; we know that aperiodicity will reduce the real efficiency, but we cannot model this effect. This limitation is not unique to the differential method; it applies to all Fourier-based methods, including the modal method. Modelling it rigorously would require the integral method or modified integral method, applied across hundreds or thousands of unique grooves. Unfortunately, existing implementations of the integral method also apply a pseudo-periodic simplification (Goray & Seely, 2002) in order to achieve adequate performance; calculations involving hundreds of unique grooves are not computationally feasible.

6.1.4. Surface roughness. As with plain mirrors, microroughness on the surface of a grating contributes to diffuse scattering and stray light (Palmer & Loewen, 2005), both in and out of the plane of incidence. Unlike mirrors, roughness on gratings also disrupts the essential periodicity of the grooves, as discussed in the previous section.

Substantial research has been devoted to modelling the effect of surface roughness, even in the simpler case of flat surfaces: Elfouhaily & Guérin (2004) categorized 260 references, 177 since 1980, into 30 different methods, before concluding that '...*there does not seem to be a universal method that is to be preferred systematically. All methods present a compromise between versatility, simplicity, numerical efficiency, accuracy and robustness, with a different weighting*

in these various fields. [...] *No approximate model has fulfilled all listed criteria.*'

For flat surfaces, two simplifications are commonly used to estimate the reduction in reflectivity as a function of the RMS surface roughness σ. The Beckmann factor (Beckmann & Spizzichino, 1987) contains a small-angle approximation that restricts it to near-normal incidence applications, but is appropriate for 'rough' surfaces up to ($\sigma \cos\theta \leq \lambda$), where θ is the incidence angle from the normal,

$$R' = R \exp\left[-\left(\frac{4\pi\sigma\cos\theta}{\lambda}\right)^2\right]. \tag{20}$$

The X-ray Data Booklet (Thompson & Vaughan, 2001) gives another correction factor based on the X-ray specific work of Sinha *et al.* (1988); it is appropriate for grazing incidence, but restricted to 'smooth' surfaces ($\sigma \ll \lambda$),

$$R' = R \exp\left\{-\left(\frac{4\pi\sigma}{\lambda}\right)^2 \sin\theta \ \mathrm{Re}\left[(\nu^2 - \sin^2\theta)^{1/2}\right]\right\}. \tag{21}$$

It is not clear that these expressions for mirror reflectivity can be applied by analogy to grating efficiencies. First, it is not obvious that surface roughness should affect all reflected orders in the same way, considering that the outgoing angles are different for each. Additionally, substantial random roughness creates groove-to-groove variations that should disrupt diffraction, beyond the simple effect of diffuse scattering. However, Goray & Seely (2002) tested the integral method without pseudo-periodic simplification over a very large number of groove periods modified by a non-Gaussian roughness distribution function. They suggest that similar results can be obtained in a feasible time by simply multiplying the outgoing field amplitudes by a factor $\exp[-(2\pi\sigma\cos\theta/\lambda)^2]$ almost identical to the Beckmann factor. This conclusion was found at near-normal incidence; for grazing-incidence gratings we have attempted to account for roughness using equation (21) instead, but we recognize that this approach is not rigorous, nor accurate for large roughness values.

6.2. Using efficiency calculations and fitting to predict real-world grating parameters

No grating can ever be manufactured exactly as specified, so we would expect the real efficiencies to be different than initially predicted. To what extent is it possible to account for the discrepancies using the differential method? Given that we have (*a*) real efficiencies measured over a range of wavelengths, (*b*) AFM measurements of the grating geometry, and (*c*) the ability to model arbitrary groove profiles, we answered this question using a curve-fitting process to generate theoretical efficiency curves that match the measurements, and then compared the fitted parameters with the actual grating parameters.

The fitting process used fixed values for the parameters that could be measured exactly. The exact groove densities had been previously determined from LTP measurements. The incidence angles measured by the diffractometer encoders

were taken as given. Because the AFM blaze angle estimates vary from groove to groove and are subject to uncertainty in the z-axis calibration, we left these (and the anti-blaze angles) as free parameters in the fitting process. The oxide layer thickness for the nickel gratings and the surface roughness parameter σ in equation (21) were also left as free parameters.

We note that a single measurement at a single wavelength would not be sufficient for this technique; we need an efficiency spectrum over wavelength. The power of the fitting process comes from the fact that each parameter (groove density, incidence angle, groove geometry, *etc.*) affects the shape of the spectrum in a different way; the spectral shape acts as a 'fingerprint' or 'hash' of the grating parameters.

Although the shapes of the measured spectra were similar to our calculated curves, the measurements were always lower than predicted in absolute value. This is reasonable based on the effects identified above that act to reduce the efficiency. However, neither of the roughness expressions [equations (21) and (20)] can describe this well on their own: both of them decrease too rapidly with increasing photon energy while providing negligible reduction at low energies, and the size of the required parameter σ ends up far outside the valid range for equation (21) ($\sigma \ll \lambda$).

Instead, it seems that a constant scaling factor is required to achieve a good fit between the measured and calculated curves. (Typical scaling values for our measurements are between 0.5 and 0.8.) Many of the causes identified above could account for the reduction, but currently we do not have a rigorous physical derivation for this factor. If it is due to roughness alone, then neither equation (21) nor equation (20) are adequate for describing gratings. The reduction could also be a measurement effect: for example, focusing or dispersion of the diffractometer beam by the spherical grating on its way to the photodiode would change the apparent intensity; sagittal tilt of the grating would cause conical diffraction and cause some light to miss the photodiode.

Reasonable fitting results can be found by using the same scaling factor for the first-order and second-order efficiencies. However, much better agreement in the shapes of the curves is found using independent scaling factors for the first-order and second-order curves. Whether this is justifiable depends on the explanation for the scaling factor; both roughness and focusing effects could be affected by the outgoing angle and hence the diffraction order.

Fitted parameters for the blaze angle, oxide thickness and RMS roughness are tabulated in Table 2. In all cases the blaze angles generated via fitting are in very close agreement with the AFM estimates. Work is ongoing to validate the oxide thickness and roughness predictions. In the following section we compare the measured and fitted (calculated) efficiency curves for each grating.

6.3. Individual grating results

6.3.1. LEG. The LEG was one of the easiest gratings to manufacture, owing to low groove density and lack of a secondary coating. The AFM measurements (Fig. 6) show a
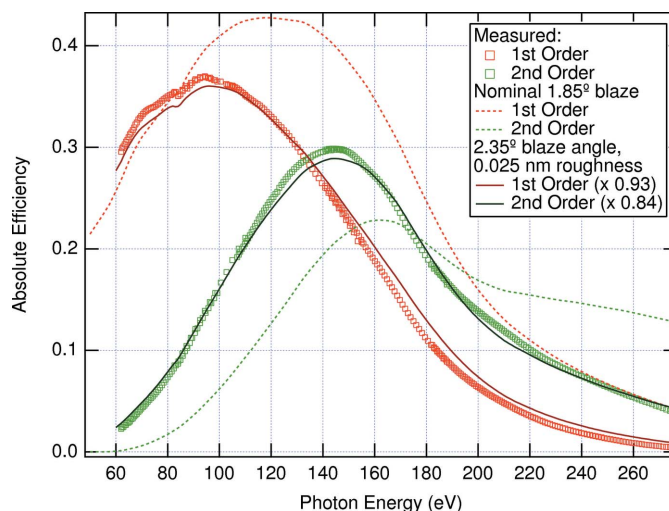

Figure 7
Measured and calculated efficiencies for the LEG. The manufactured blaze angle is higher than requested, which shifts the efficiency peaks to lower energies and transfers energy to the second order. (Dashed lines are calculations based on the nominal parameters we requested from the manufacturer. Solid lines are the result of using a curve-fitting process to determine the grating parameters that best match the measured curves.)

clean triangular profile; however, we estimate from these measurements that the blaze angle at the centre of the grating is $2.45° \pm 0.20°$ instead of the requested $1.85°$.

The effect of the blaze angle error on the measured efficiency is obvious in Fig. 7: the locations of the efficiency peaks are shifted compared with the theoretical prediction for a nominal grating with $1.85°$ blazing. The higher blaze angle also increases the second-order peak efficiency at the expense of the first.

By matching the calculated to the measured spectra, our fitting process predicts a blaze angle of $2.35°$, using scaling factors of 0.93 and 0.84 for the first and second orders, respectively. The agreement in the shape of the curves is very good (Fig. 7), and the predicted blaze angle agrees closely with the AFM estimate ($2.45°$). The high scaling factors compared with the IMP and MEG gratings suggest low roughness; it makes sense that this bare gold grating would be smoother than the over-coated gratings.

Although only a fraction of a degree, the blaze angle error causes a significant reduction in real efficiency: at 140 eV, the theoretical and measured first-order efficiency is less than 0.3, compared with 0.4 that could be achieved with correct blazing. Fortunately, this is still high compared with the other gratings and should be acceptable for all experiments.

6.3.2. IMP. The AFM measurements of the impurity grating show clean facets on the blazed side (Fig. 6), although once again the blaze angle is $\sim 0.5°$ higher than specified. The estimated blaze angle at the grating centre is $1.60° \pm 0.11°$ compared with the requested $1.11°$.

Originally intended to cover the range from 200 to 800 eV, the IMP grating suffers a drop in real efficiency near 540 eV (Fig. 8). The fact that this occurs at the oxygen absorption edge (543 eV) strongly suggests an oxide layer on the surface.
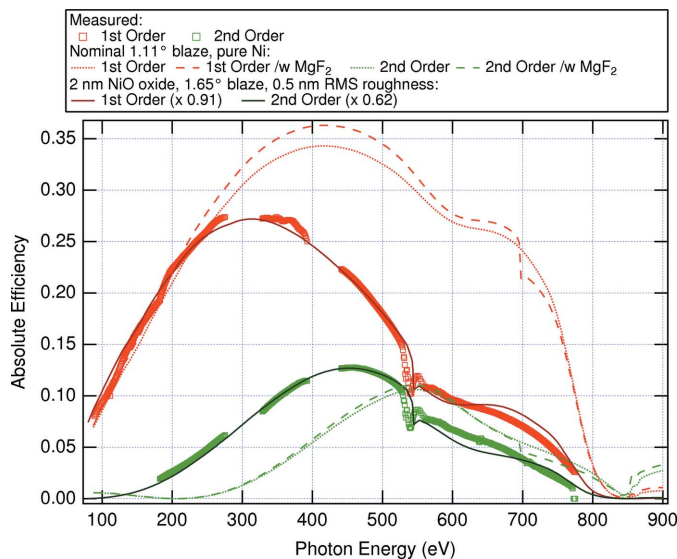
Figure 8
Measured and calculated efficiencies for the IMP grating. The difference between the nominal and actual efficiency is explained by a higher blaze angle (1.65° instead of 1.11°), the presence of a 2.0 nm oxide layer, and 0.5 nm RMS surface roughness. A 1 nm MgF₂ coating (dashed lines) could have protected the grating from oxidation.
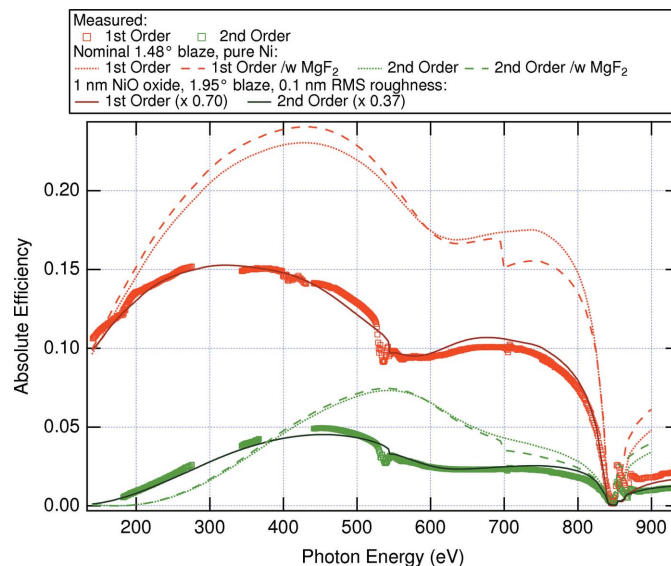

Figure 9
Measured and calculated efficiencies for the MEG grating. The difference between the nominal and actual efficiency is explained by a higher blaze angle (1.95° instead of 1.48°), the presence of a 1.0 nm oxide layer, and 0.1 nm RMS surface roughness. A 1 nm MgF₂ coating (dashed lines) could have protected the grating from oxidation.

We modelled this using a layer of NiO of unknown thickness over a nickel substrate. The fitting results suggest that the measured efficiencies can be explained very well using a 2.0 nm oxide layer, a blaze angle of 1.65°, a 5° anti-blaze angle, an RMS roughness of 0.5 nm, and scaling factors of 0.91 and 0.62, respectively (Fig. 8). Again, the blaze angle predicted from fitting falls well within error of the AFM estimate (1.60°).

As mentioned in §2.5, we should not expect the Henke-based refractive indexes to be accurate near the oxygen and nickel edges around 543 and 853 eV; in particular, the EXAFS profile is absent in the calculated spectra above the edge.

6.3.3. MEG. Owing to its increased groove density of 1200 lines mm⁻¹, the MEG shows a less regular surface than either the LEG or IMP. AFM measurements of the profile (Fig. 6) estimate an average blaze angle of 2.04° ± 0.22° at the centre of the grating. Once again, this is consistently 0.5° higher than the nominal specification (1.48°).

The nickel-coated MEG suffers the same fate as its oxidized sibling. The measured efficiency (Fig. 9) is further affected by the error in the blaze angle. The fitting process predicts a blaze angle of 1.95°, an NiO oxide layer of 1 nm, and scaling factors of 0.70 (first order) and 0.37 (second order). The lower scaling factors are likely attributed to the groove-to-groove variation visible in the AFM profile, which is significant compared with the LEG and IMP grating. Once again, the fitted blaze angle agrees closely with the AFM estimate (2.04°).

6.3.4. HEG. Measurements of the HEG show that the efficiency spectrum is dramatically lower than predicted across the entire energy range (Fig. 10). The AFM measurements (Fig. 6) clearly reinforce that something went very wrong in the ruling process. At the centre of the grating there is a double-peaked structure, and the dimensions differ substantially from groove to groove. We know that the HEG blank

was re-ruled after a previous failed attempt, and we hypothesize that some structure was left over from the first ruling.

Could the double-peaked shape of the HEG grooves be responsible for its poor efficiency? To answer this question we used the arbitrary profile mode of the new software. We extracted a representative shape from one of the AFM grooves and used it to specify the set of (x, y_p) points for the profile function $y_p = g(x)$.

The efficiencies calculated from this profile are also shown in Fig. 10. While the double-peaked shape does reduce the
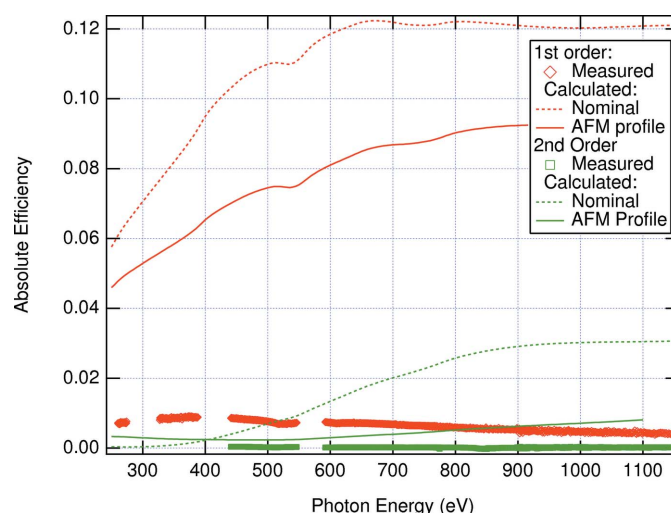

Figure 10
The HEG grating efficiency was measured to be extremely low. AFM measurements suggest that this might be due to a non-triangular profile and strong variation from groove to groove (Fig. 6). Calculations (solid lines) using a representative groove shape taken from one period of the AFM measurements cannot fully explain the reduced efficiency, owing to significant groove-to-groove variation.

theoretical efficiency compared with the nominal profile, it cannot explain the near-zero efficiencies that we measured. Instead, we attribute this to the substantial aperiodic variation from groove to groove, which disrupts the proper formation of diffracted plane waves. (In the limit of complete random variation from groove to groove, the grating simply reduces to a diffuse scattering surface.)

This grating highlights the practical importance of characterization. Without efficiency and AFM measurements, we would have accepted and installed this grating in the spectrometer, but this version of the HEG would have been unusable. Instead, we used the characterization data to ask the manufacturer to re-rule it one more time.

6.3.5. HRMEG and HRHEG. The high-resolution third-order gratings were also characterized using AFM and diffractometer measurements. Unfortunately, the efficiency measurements were affected by an error in the diffractometer control software, causing problems with the normalization. It might be possible to correct this problem in post-processing, but currently the full efficiency spectra are not ready for publication. We include summary results taken from the valid measurement points here.

The nickel-coated HRMEG has a measured third-order efficiency peak of 3.5%, but unfortunately the peak occurs at 500 eV instead of the 285 eV design energy. Like the other two nickel gratings, it shows fine structure and a serious decrease in efficiency at the oxygen edge (543 eV). AFM measurements of the HRMEG profile show a beautiful triangular structure (Fig. 6); unfortunately the blaze angle is $4.43° ± 0.30°$ instead of $4.85°$ at the centre of the grating. Unlike the other gratings, this is $0.4°$ lower than requested. The blaze angle error explains why the measured efficiency peak is shifted to higher energy compared with the nominal calculations. The effect on the spectrometer performance is almost a factor of two: instead of >3% third-order efficiency that could be achieved at 285 eV with proper blazing, we obtain only 1.5%.

For the HRHEG, AFM measurements show a rough profile and an extremely high blaze angle of $6.34° ± 0.28°$, more than $2°$ higher than the required $4.05°$. Accurate blazing is essential for exploiting the third-order efficiency peak, so it was unfeasible to use this grating in the role we originally designed: the third-order efficiency is less than 0.5% at 400 eV, and decreases to 0.28% at the design energy of 710 eV.

However, the blaze angle error contained a lucky coincidence: it actually makes the HRHEG ideally blazed for first-order operation from 400 eV to 900 eV. (Owing to the extreme groove density, the first-order efficiencies are low but usable: it was measured to provide 2% efficiency at 400 eV, and >1% efficiency at 800 eV.) Simultaneously, the failure of the HEG left us lacking a first-order grating for experiments above 530 eV. Therefore, we installed the HRHEG in the spectrometer as a temporary first-order HEG replacement until the manufacturer completes re-ruling of the actual HEG. A corrected version of the HRHEG will be re-ruled and measured in the future. This example highlights again the usefulness of careful grating characterization from an engineering perspective.

7. Conclusions

To summarize, we have used insights from rigorous grating efficiency calculations to design a high-performance soft X-ray emission spectrometer, which intelligently navigates the inherent trade-off between resolution and efficiency. We identify and exploit a principle of optimal incidence angle, and use blazed gratings optimized for third-order operation to achieve higher resolution than would otherwise be possible within the space constraints of the machine.

In order to model real gratings with arbitrary profiles, and increase the computational performance of efficiency calculations, we implement new open-source software for calculating efficiencies using the differential method. A simple online application is provided at http://www.dgembe.com/ so that beamline designers can quickly evaluate the efficiency of a proposed design; they can also download the command-line version for automation, optimization or integration into other applications.

Finally, we compare measurements and calculations of grating efficiency as a function of wavelength. We find that the differential method accurately describes the shape of efficiency spectra for typical grazing-incidence gratings once real-world effects are accounted for (geometry errors, oxide thickness and surface roughness). Because different grating parameters affect the shape of efficiency curves in different ways, we find that it is actually possible to predict unknown grating parameters based on efficiency measurements, using a curve-fitting process to 'invert' the calculations. For all the gratings we analyzed, the blaze angles predicted through fitting agree very closely, within error, with AFM measurements of the actual groove profiles. In the future, this might provide a way to characterize grating parameters that are difficult or impossible to measure directly.

References

Andrewartha, J., Derrick, G. & McPhedran, R. (1981). *Opt. Acta*, **28**, 1501–1516.

Beckmann, P. & Spizzichino, A. (1987). *The Scattering of Electromagnetic Waves from Rough Surfaces.* Boston: Artech House.

Botten, L., Craig, M., McPhedran, R., Adams, J. & Andrewartha, J. (1981). *Opt. Acta*, **28**, 1087–1102.

Bowler, M., Finetti, P., Holland, D., Humphrey, I., Quinn, F. & Roper, M. (2001). *Nucl. Instrum. Methods Phys. Res. A*, **467**, 317–320.

Byrne, G. D. & Hindmarsh, A. C. (1975). *ACM T. Math. Softw.* **1**, 71–96.

Elfouhaily, T. M. & Guérin, C.-A. (2004). *Wave. Random Media*, **14**, R1–R40.

Ghiringhelli, G., Piazzalunga, A., Dallera, C., Trezzi, G., Braicovich, L., Schmitt, T., Strocov, V. N., Betemps, R., Patthey, L., Wang, X. & Grioni, M. (2006). *Rev. Sci. Instrum.* **77**, 113108.

Goray, L. (2005). *Nucl. Instrum. Methods Phys. Res. A*, **536**, 211–221.

Goray, L. I. & Seely, J. F. (2002). *Appl. Opt.* **41**, 1434–1445.

Harada, Y., Kobayashi, M., Niwa, H., Senba, Y., Ohashi, H., Tokushima, T., Horikawa, Y., Shin, S. & Oshima, M. (2012). *Rev. Sci. Instrum.* **83**, 013116.

Henke, B., Gullikson, E. & Davis, J. (1993). *At. Data Nucl. Data Tables*, **54**, 181–342.

Jark, W. (1988). *Nucl. Instrum. Methods Phys. Res. A*, **266**, 414–421.

Jark, W. & Nevière, M. (1987). *Appl. Opt.* **26**, 943–948.

Johnson, R. L. (1978). *Nucl. Instrum. Methods*, **152**, 117–122.

Li, L. (1996a). *J. Opt. Soc. Am. A*, **13**, 1024–1035.

Li, L. (1996b). *J. Opt. Soc. Am. A*, **13**, 1870–1876.

Maystre, D. (1972). *Opt. Commun.* **6**, 50–54.

Maystre, D. & McPhedran, R. (1974). *Opt. Commun.* **12**, 164–167.

Nevière, M., (2003). *GRADIF.* Contact: m.neviere@free.fr.

Nevière, M., Flamand, J. & Lerner, J. (1982). *Nucl. Instrum. Methods Phys. Res.* **195**, 183–189.

Nevière, M. & Montiel, F. (1996). *Proc. SPIE*, **2805**, 176–183.

Nevière, M. & Popov, E. (2003). *Light Propagation in Periodic Media: Differential Theory and Design.* New York: Marcel Dekker.

Nevière, M., Vincent, P. & Petit, R. (1974). *Nouv. Rev. Opt.* **5**, 65.

Padmore, H., Martynov, V. & Holis, K. (1994). *Nucl. Instrum. Methods Phys. Res. A*, **347**, 206–215.

Palmer, C. & Loewen, E. (2005). *Diffraction Grating Handbook*, 6th ed. Newport Corporation. (Also available online at http://gratings.newport.com/library/handbook/handbook.asp.)

Pomp, A. (1991). *J. Mod. Opt.* **38**, 109–120.

Popov, E. & Nevière, M. (2000). *J. Opt. Soc. Am. A*, **17**, 1773–1784.

Popov, E. & Nevière, M. (2001). *J. Opt. Soc. Am. A*, **18**, 2886–2894.

Sinha, S. K., Sirota, E. B., Garoff, S. & Stanley, H. B. (1988). *Phys. Rev. B*, **38**, 2297–2311.

Thompson, A. C. & Vaughan, D. (2001). *X-ray Data Booklet*, 2nd ed. Lawrence Berkeley National Laboratory, University of California, USA. (Also available online at http://xdb.lbl.gov/).

Underwood, J. H., Gullikson, E. M., Koike, M., Batson, P. J., Denham, P. E., Franck, K. D., Tackaberry, R. E. & Steele, W. F. (1996). *Rev. Sci. Instrum.* **67**, 3372.